POLITECNICO DI TORINO
Repository ISTITUZIONALE

Novel green-engineered hierarchical PLA-Ag nanohybrids for antimicrobial environmental purification

*Original*
Novel green-engineered hierarchical PLA-Ag nanohybrids for antimicrobial environmental purification / Gattucci, Francesca; Maio, Andrea; Lallukka, Mari Sofia; De Boni, Francesco; Prato, Mirko; Scaffaro, Roberto; Miola, Marta. - In: ADVANCED COMPOSITES AND HYBRID MATERIALS. - ISSN 2522-0136. - 9:(2026), pp. 1-15. [10.1007/s42114-026-01733-7]

*Availability:*
This version is available at: 11583/3009408 since: 2026-03-30T15:11:25Z

*Publisher:*
Springer

*Published*
DOI:10.1007/s42114-026-01733-7

*Terms of use:*

This article is made available under terms and conditions as specified in the corresponding bibliographic description in the repository

*Publisher copyright*

(Article begins on next page)

26 April 2026

Advanced Composites and Hybrid Materials (2026) 9:187
https://doi.org/10.1007/s42114-026-01733-7

RESEARCH

# Novel green-engineered hierarchical PLA-Ag nanohybrids for antimicrobial environmental purification

**Francesca Gattucci[1] · Andrea Maio[2] · Mari Sofia Lallukka[1] · Francesco De Boni[3] · Mirko Prato[3] · Roberto Scaffaro[2] · Marta Miola[1]**

Received: 7 November 2025 / Revised: 18 February 2026 / Accepted: 2 March 2026
© The Author(s) 2026

**Abstract**
The development of sustainable antimicrobial materials is essential for next-generation air and water purification systems, particularly in view of the increasing occurrence of multidrug-resistant pathogens. In this work, three-dimensional porous poly(lactic acid) (PLA) fibrous mats were fabricated by coagulation-wet electrospinning, followed by pH-controlled in situ green functionalization with silver (Ag) and silver oxide ($Ag_2O$) nanoparticles using tannic acid as a natural reducing agent. The influence of pH on nanoparticle nucleation, size, distribution, and composition was systematically investigated. Comprehensive surface and structural analyses (ATR-FTIR, FE-SEM, EDS, XRD, XPS) were performed immediately after functionalization and after 30 days of immersion in water to simulate realistic filtration conditions. The results confirmed successful and stable incorporation of silver species and revealed pH-dependent differences in nanoparticle characteristics. Antibacterial tests against *Staphylococcus epidermidis and Escherichia coli* showed strong efficacy with significant retention of activity after prolonged water exposure. Uniaxial compression tests performed in aqueous conditions demonstrated that the monoliths possess sufficient mechanical robustness and structural integrity for water filtration applications. Antibacterial water filtration test evidenced a significant removal of *S. epidermidis* and a complete inactivation of the bacteria on the silver-containing filters. Overall, pH-tailored Ag-functionalized PLA fibrous scaffolds emerge as a sustainable, durable, and effective platform for antimicrobial environmental purification.

**Keywords** Wet electrospinning · PLA · Antibacterial · Silver nanoparticles · Green synthesis

## 1 Introduction

Microbial contamination remains a major transmission route for infections and continues to pose a significant threat to public health [1, 2]. While antibiotics are a primary method for combating bacterial infections, their widespread and inappropriate use has led to the emergence of multidrug-resistant strains, recognized by the World Health Organization (WHO) as a global health emergency [3]. As treatment options become increasingly limited, preventing exposure to infectious agents has become a critical public health strategy.

Clean air and water are fundamental to health protection in both medical and community environments [4, 5]. Contaminated water can serve as a vehicle for bacteria, viruses, and protozoa, leading to disease outbreaks even in developed countries [6]. Similarly, airborne pathogens can spread through droplets or aerosols [7], as demonstrated by the COVID-19 pandemic [8]. In response, the WHO has advocated for the use of air purification systems and personal protective equipment to mitigate airborne transmission risks [9]. Additionally, pollutants such as particulate matter (PM) and volatile organic compounds (VOCs) not only impair respiratory function [10], but also support microbial adhesion, biofilm formation, and increased infectivity [11].

✉ Roberto Scaffaro
roberto.scaffaro@unipa.it

✉ Marta Miola
marta.miola@polito.it

[1] Department of Applied Science and Technology, Politecnico di Torino, Corso Duca degli Abruzzi 24, Turin 10129, Italy

[2] Department of Engineering, University of Palermo, Viale delle Scienze Ed. 6, Palermo 90128, Italy

[3] Istituto Italiano di Tecnologia, Via Morego 30, Genova 16163, Italy

Published online: 20 March 2026

Filtration is a widely adopted approach for removing contaminants from air and water streams [12–14]. Fibrous filters, particularly those fabricated through electrospinning, are prized for their high porosity and extensive surface area [15, 16]. However, these filters may become saturated over time, promoting bacterial colonization and biofilm development, risks that are especially concerning for immunocompromised individuals. To address this issue, the incorporation of antibacterial functionalities into filters [17] and electrospun membranes offers a promising route to enhance filter performance and safety [18].

Among the polymers potentially suitable as fibrous substrates, poly(lactic acid) (PLA) is one of the most promising. It is a biodegradable polyester derived from renewable resources, whose proven electrospinnability makes it widely used for producing 2D mats. Surprisingly, however, the possibility to process PLA into fibrous fluffy scaffolds via wet electrospinning – that is, using a liquid collector instead of a solid one – is still scarcely explored, although this emerging technique enables the rapid fabrication of 3D porous monoliths with precise control over their nano- and microscale architecture by adjusting processing parameters and the characteristics of coagulation bath [19, 20]. In this latter context, the proper design of fluffy fibrous structures is crucial for obtaining materials that are mechanically flexible and lightweight, while also ensuring a high surface area for the deposition of active nanoparticles that enhance long-term antimicrobial effectiveness.

Silver and its compounds have long been recognized for their potent antimicrobial properties [21]. The antibacterial efficacy of silver nanoparticles (AgNPs) is primarily attributed to the release of $Ag^+$ ions and the nanoparticles' high surface reactivity, enabling them to interact with and disrupt bacterial cell membranes, leading to cell death [22]. These silver ions can bind to bacterial membranes, impairing energy production by disrupting ATP synthesis, and interfere with DNA replication. Additionally, they promote the generation of reactive oxygen species (ROS), which further contributes to cellular damage [23]. While the complete mechanisms are still under investigation, AgNPs have also demonstrated antiviral activity, including effectiveness against SARS-CoV-2, highlighting their potential in reducing viral transmission [24].

With the increasing demand for sustainable technologies, green synthesis of AgNPs has emerged as a widely explored alternative to conventional chemical routes. This approach relies on natural reducing agents, particularly plant extracts enriched with bioactive phytochemicals, to convert silver ions into nanoparticles under non-toxic conditions [25] and low temperature processes. While various plant-derived compounds have been involved in the green synthesis of metal nanoparticles, polyphenols are the most prominent contributors, owing to their strong electron-donating capacity and their ability to enhance the stability of the resulting nanomaterials [26].

Tannins are phenolic substances commonly found throughout a wide variety of plant species [27]. Among these, tannic acid is particularly notable for its strong antioxidant capacity [28] and its effective ability to reduce metal ions, especially under basic pH conditions, and to stabilize the resultant nanoparticles without increasing the temperature [29]. In addition, tannic acid exhibits antibacterial effects against selected microbial strains [30], suggesting its potential to enhance the overall antimicrobial efficacy of AgNP-based systems.

The in situ green reduction approach has also been successfully applied to fibrous materials [31]. In this study, fibrous poly(lactic acid) (PLA) mats were fabricated using wet electrospinning and then functionalized via an in situ green reduction process employing tannic acid, previously evaluated by the authors for its effectiveness as a natural reducing agent [32]. Given that the reductive capacity of tannic acid is strongly influenced by pH [33], two different pH conditions were employed to assess their impact on nanoparticle formation. The stability and antibacterial performance of the functionalized fibers were then evaluated following prolonged immersion in water, to simulate conditions relevant to filtration and humid environments together along with an antibacterial water filtration test using a bench-scale dead-end filtration model system.

## 2 Materials and methods

### 2.1 Materials

Polylactic acid (PLA) used in this work was a commercial sample of Ingeo 2003 D (NatureWorks), having a content of D-LA monomer equal to ~4%, density (ρ) = 1.24 g/cm$^3$, melt flow index (MFI) = 6 g/10 min, melting temperature (Tm) = 160 °C, and Mw = 240 kDa. Tannic acid (TA) was used as a reducing agent for the green reduction in situ of the silver nanoparticles (AgNPs) and silver nitrate ($AgNO_3$) was used as the silver source in the process. Potassium carbonate ($K_2CO_3$) and sodium hydroxide (NaOH) were used to maintain alkaline pH during the process. All reactants were purchased by Merck (Darmstadt, Germany).

### 2.2 One step preparation of PLA fluffs

To fabricate the fibrous fluffs, a vertical electrospinning setup was designed with a liquid collector serving as a coagulation bath (Fig. 1a). A 10 wt% PLA solution was prepared by dissolving PLA in a chloroform/acetone (2:1

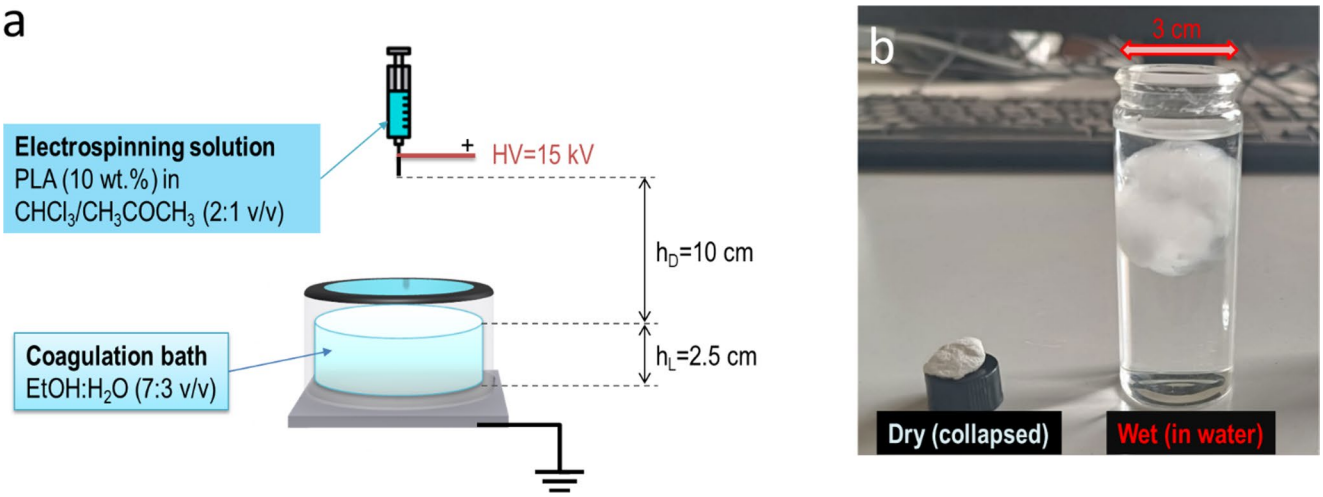


**Fig. 1** Schematics of the coagulation-wet electrospinning process (**a**); digital photograph of a collapsed dry fluff and an expanded wet fluff stored in distilled water (**b**)

v/v) mixture under stirring. The solution (30 mL) was then loaded into a glass syringe fitted with a 19G stainless steel needle and processed via dry jet wet electrospinning into an ethanol/water (7:3 v/v) coagulation bath.

The electrospinning parameters were set as follows: 15 kV voltage, 3 mL/h flow rate, 10 cm dry jet height ($h_D$), 2.5 cm liquid height ($h_L$), and 15 min of electrospinning per batch. The resulting wet fluffy monoliths were promptly transferred to deionized water to prevent collapse (Fig. 1b).

This technique, known as coagulation-wet electrospinning, is highly effective for rapidly fabricating fibrous materials with a multiscale design [19, 20]. While fiber diameter can be controlled by tuning the electrospinning parameters, as in conventional electrospinning processes, the careful selection of the coagulation bath composition enables control over the three-dimensional fiber arrangement and pore architecture. In this case, 70:30 ethanol/water bath was selected as a compromise between surface tension and phase separation rate. In fact, the ethanol lowers the surface tension, allowing the fibres to sink and arrange in a three-dimensional structure, while the water content is sufficient to accelerate solvent exchange and phase separation, promoting porosity in the PLA fibres, with desirable increase of surface area in view of the subsequent functionalization.

## 2.3 Functionalization with tannic acid (PLA-TA)

The protocol for the functionalization was adapted for the in situ reduction of nanoparticles from a previous work of Kodadaddi et al. [34] that was already established by the authors in the reduction in situ of silver nanoparticles on natural zeolite clinoptilolite [32]. The PLA fluff was transferred from deionized water, where it was kept, to a 0.006 M tannic acid aqueous solution and buffered with $K_2CO_3$ aqueous solution at pH 8.5. The fluff was maintained on a roller for 24 h to let the functionalization happen and then rinsed in Milli-q water.

## 2.4 Functionalization with silver (PLA-TA-Ag)

The PLA-TA fluff was transferred to a silver nitrate 0.5 M aqueous solution. Two types of functionalization were applied, A and B, to estimate the effect of pH variation on nanoparticle formation. In the functionalization A the PLA-TA fluff after being immersed in the silver nitrate solution was kept on a roller for 24 h while in the functionalization B the PLA-TA fluff immersed in the silver nitrate solution underwent a buffering with sodium hydroxide solution at pH 8.5 similarly to what was done for the reduction in situ on clinoptilolite by the authors [32]. The entire functionalization process is reported in Fig. 2. Both samples were subsequently stored in Milli-Q water for 30 days and labeled as PLA-TA-Ag A 30d and PLA-TA-Ag B 30d, respectively.

## 2.5 Sample characterization

### 2.5.1 Physicochemical characterization

PLA characterization followed every step of the functionalization, first with tannic acid, later with silver. Attenuated Total Reflectance Fourier-Transform Infrared spectroscopy (ATR-FTIR, Nicolet iS 50 Spectrometer (Thermo Scientific, Milan, Italy)) was utilized to characterize the chemical composition and bonding on PLA with tannic acid. Morphological characterization was conducted through Field-Emission Electron Microscopy (FESEM-EDS SUPRATM 40, Zeiss and Merlin Gemini Zeiss). Compositional analyses were carried out using energy dispersive spectroscopy (EDS,

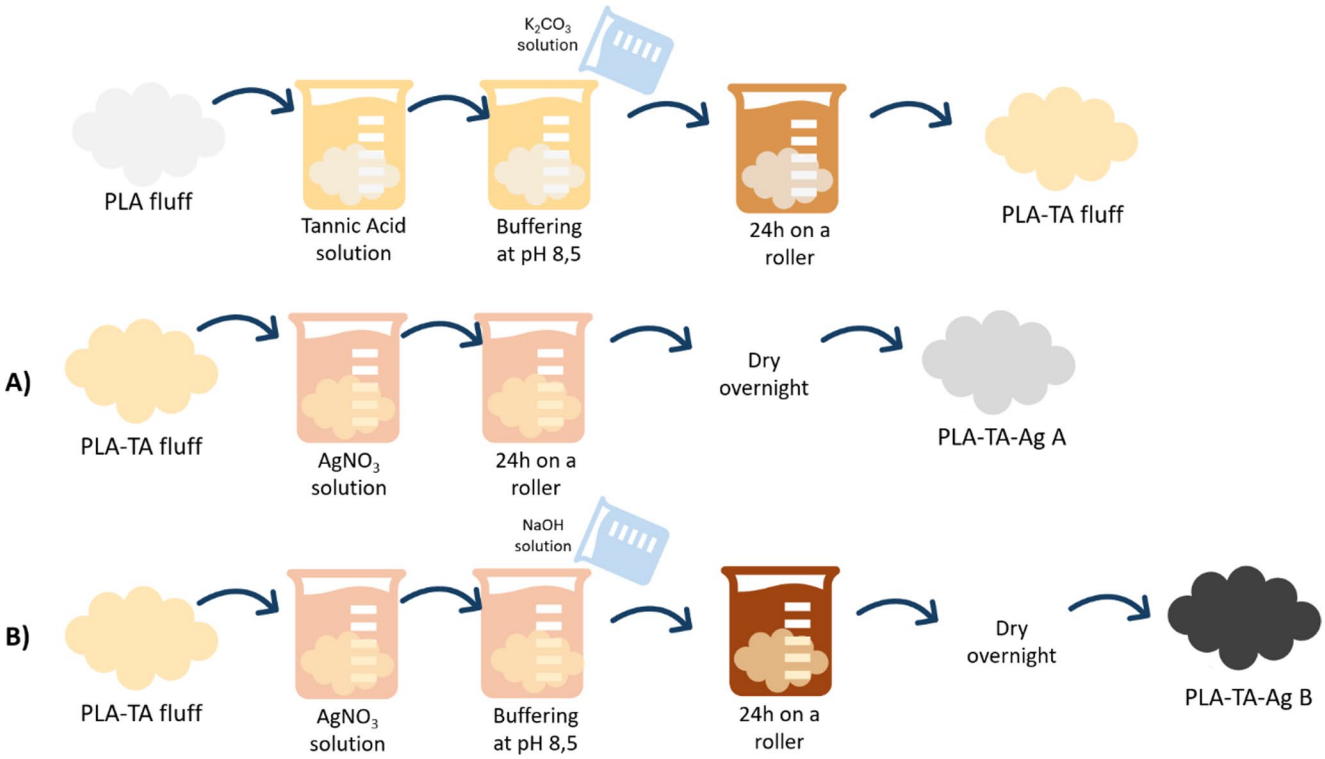


**Fig. 2** Schematics of the green route followed to functionalize PLA with Tannic Acid and silver

EDAXPV 9900TM) and X-rays photoelectron spectroscopy (XPS). X-rays photoelectron spectroscopy (XPS) measurements were carried out through a Kratos Axis Ultra$^{DLD}$ spectrometer (Kratos Analytical Ltd.) with a monochromated Al $K_\alpha$ X-ray source ($hv$ = 1486.6 eV) operating at 20 mA and 15 kV. Each specimen was prepared by pressing some µg of the sample onto an indium substrate until producing a homogeneous film. The wide scans were collected over an analysis area of 300 × 700 µm$^2$ at a photoelectron pass energy of 160 eV and energy step of 1 eV, while Ag Auger, Ag 3d, C 1s, and O 1s high-resolution spectra were collected at a photoelectron pass energy of 10 eV and an energy step of 0.1 eV, corresponding to an instrumental resolution of 0.26 eV. A take-off angle of 0° with respect to the sample normal direction was used for all analyses. The differential electrical charging effects observed on all samples were neutralized. The spectra have been calibrated to the PLA C-C component of the carbon 1s peak at 284.8 eV, except for the spectra of the standard metallic Ag specimen, which have been calibrated to the Fermi edge at 0 eV. The spectra were analyzed with the CasaXPS software (Casa Software Ltd., version 2.3.25) [35] and the residual background was eliminated by the Shirley method across the binding energy range of the peaks of interest. The relative atomic concentrations were then estimated using the specific function in the CasaXPS software. The characterization in terms of the samples' structure was performed using X-ray diffractometry (XRD, Bragg–Brentano X'pert Philips diffractometer) using the Bragg Brentano camera geometry and the Cu-Ka incident radiation. The 2θ range used for sample measurements was from 20° to 80°. Analysis of the obtained pattern werer performed with X'Pert HighScore software, referencing the PCPDF database.

All characterizations were performed on the PLA-TA-Ag A and B samples, as well as after 30 days of immersion in Milli-Q water (PLA-TA-Ag A 30d and PLA-TA-Ag B 30d). The water in which the samples were stored for 30 days was analyzed to assess the release of silver ions. Each sample was immersed in 5 mL of water, which was subsequently diluted fivefold before analysis. Silver ion concentrations, expressed in parts per million (ppm), were measured using a spectrophotometer (Hanna Instruments).

### 2.5.2 Antibacterial activity evaluation

The preliminary antibacterial efficacy of PLA samples was assessed through the zone of inhibition test according to the NCCLS M2-A9 [36] performance standard using non-pathogenic strains of *Staphylococcus epidermidis* (Gram-positive, ATCC14990) and *Escherichia coli* (Gram-negative, ATCC8739). The bacterial solutions (McFarland index 0.5) were spread on Mueller Hinton and Nutrient agar plates. PLA, PLA-TA-Ag A, PLA-TA-Ag B, PLA-TA-Ag A 30d and PLA-TA-Ag B 30d samples were placed onto

the agar plates and incubated at 35 °C for 24 h. After the incubation, the formation of a halo was observed around the samples. The samples were incubated for an additional 24 h to evaluate the stability of the formed halo.

#### 2.5.3 Mechanical testing in water

Mechanical tests in compression mode were performed in water at T = 25 °C by means of a dynamometer (Instron 3365, U.K.) equipped with a 1 kN load cell and a BioPuls Bath (Norwood, USA). Measurements were carried out in triplicate on cylindrical specimens (diameter = 4 mm and height = 5.5 mm) compressed until failure at a constant crosshead speed of 1 mm/min. The initial elastic modulus ($E_0$) was determined from the slope of the linear fit of the stress-strain curve in the initial quasi-linear region (0–10% strain). The densification modulus ($E_F$) was obtained from the slope of the linear fit in the final densification region. The intersection of these two linear fits was used to identify the densification onset coordinates ($\varepsilon_D$ and $\sigma_D$). The maximum stress ($\sigma_{max}$) and strain ($\varepsilon_{max}$) were directly extracted from the stress-strain curves. The energy absorbed during compression was calculated by numerical integration of the area under the stress-strain curve. Furthermore, in view of water filtration applications, the strain corresponding to typical operating pressures (0.5–0.6 bar) was determined to assess the structural integrity of the materials under service conditions. Data were reported as mean value ± SD.

#### 2.5.4 Antimicrobial water filtration test

Antibacterial water filtration test was performed on PLA, PLA-TA-Ag A, and PLA-TA-Ag B using a non-pathogenic *Staphylococcus epidermidis* strain (ATCC 14990). The experiment followed the protocol reported by *Park et al.* [37]. Deionized water was autoclaved and inoculated with a bacterial suspension to obtain a final concentration of $5 \times 10^5$ colony-forming units (CFU)/mL. Starting from 20 mL, successive aliquots of contaminated water were filtered using a dead-end filtration setup (total filtered volume: 100 mL; TMP: 0.6 bar). For each 20 mL fraction, bacteria in the filtrated water were quantified by plating on Columbia blood agar and incubating at 35 °C for 24 h. The log reduction value (LRV) was calculated as:

$$LRV = -log_{10}\left(\frac{C_f}{C_0}\right)$$

where $C_0$ is the initial bacterial concentration in the feed and $C_f$ is the bacterial concentration in the filtrate. After filtration, the samples (PLA, PLA-TA-Ag A, and PLA-TA-Ag B) were recovered, placed onto Mueller–Hinton agar plates, and incubated at 35 °C for 24 h to assess bacterial growth on the filter surfaces. The release of $Ag^+$ during the filtration test was quantified by analyzing the collected filtrate using Inductively Coupled Plasma Mass Spectrometry (ICP-MS, Thermo Scientific iCAP™ Q ICP-MS). All experiments were performed in triplicate to ensure reproducibility.

## 3 Results

### 3.1 Physiochemical characterization of PLA-TA-Ag A and PLA-TA-Ag B

Figure 3 presents the ATR-FTIR analysis. The characteristic bands of PLA film, observed at 1750, 1180, 1082, and 1043 $cm^{-1}$, represent the ester backbone of PLA and are clearly visible in the FTIR spectra [38]. Additionally, the strong peak at 1753 $cm^{-1}$, corresponding to the -C = O stretching in PLA, is also present in the composite membrane [39]. The grafting of tannic acid onto PLA is confirmed in the PLA-TA spectrum, as indicated by distinct absorbance peaks related to the C = O and C-O stretching of quinic acid esters located at 1718 and 1220 $cm^{-1}$, respectively. Furthermore, the features between 1600 and 1400 $cm^{-1}$ correspond to aromatic units [40]. These characteristic peaks effectively demonstrate the effectiveness of PLA fibers functionalization with tannic acid.

After confirming the successful functionalization with tannic acid using FTIR analysis, the morphology of the samples was characterized through field emission electron microscopy (FE-SEM), as reported in Fig. 4.

The PLA exhibits a three-dimensional arrangement of fibers having a rough texture and a narrow diameter

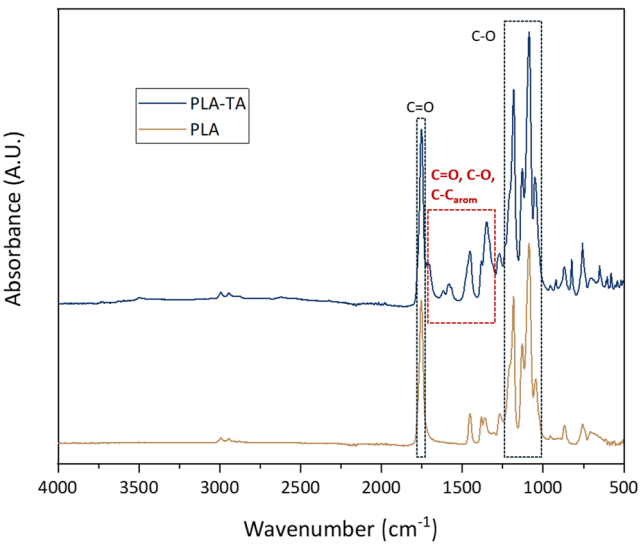


**Fig. 3** FTIR spectra of PLA before and after the functionalization with tannic acid (PLA-TA)

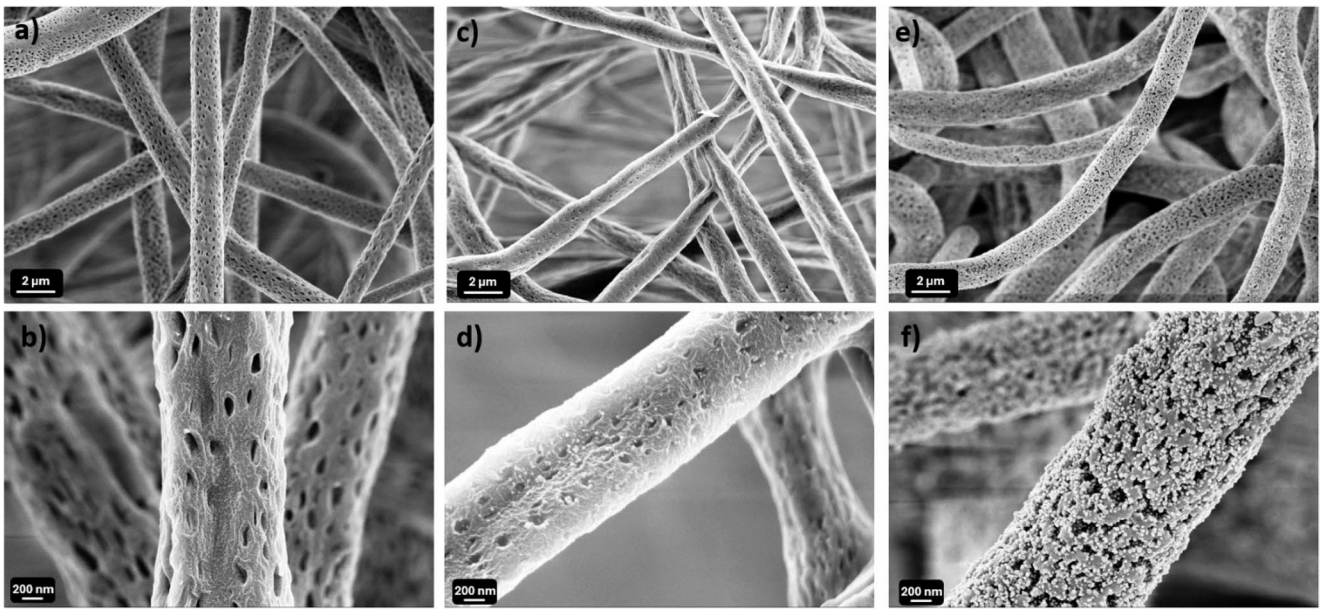


**Fig. 4** FESEM images of PLA (**a**, **b**), PLA-TA-Ag A (**c**, **d**) and PLA-TA-Ag B (**e**, **f**) taken at different magnifications

distribution, with a mean value of 1.29 µm (see Fig. S1a, supporting information). The fibers display a spongy structure, characterized by plenty of pores having 45 nm mean diameter (Fig. S1b). Nanometric cavities result from the phase separation induced by the presence of water in the coagulation bath during wet electrospinning process and are advantageous for all applications that require increased surface areas. Upon silver functionalization, nanoparticles were observed on the surface of the fibers in both cases. Following the first type of functionalization (A), the nanoparticles appeared small and well-distributed (Fig. 4c, d), while in the sample PLA-TA-Ag B, the nanoparticles were larger and more densely decorating the fibers, including within the pores (Fig. 4e, f). This could be attributed to the enhanced reducing properties of tannic acid at an alkaline pH [41]. Additionally, the porosity of the fibers appears increased after the functionalization B; this is probably due to the contact with the NaOH solution during the functionalization process that can cause a partial hydrolysis of the PLA fibers [42, 43].

EDS analysis was performed on the PLA-TA-Ag A and PLA-TA-Ag B samples, and the results are shown in Table 1. The silver concentration is approximately 0.5 at% in the PLA-TA-Ag A sample, while it reaches nearly 8 at% after the second functionalization method; this result is comparable with what was previously obtained by the authors [32]. This is likely due to the fact that the reducing properties of polyphenols are pH-dependent: an alkaline pH promotes silver functionalization, as more hydroxyl groups become deprotonated and can attract a greater number of silver ions [41]. The introduction of silver through in situ reduction is thus enhanced at higher pH levels. These results are consistent with those obtained from morphological analysis.

**Table 1** EDS analysis on PLA-TA-Ag A and PLA-TA-Ag B

| PLA-TA-Ag A | | PLA-TA-Ag B | |
|---|---|---|---|
| Element | % at | Element | % at |
| C | 43.7±2.5 | C | 31.1±4.5 |
| O | 55.8±2.4 | O | 61.2±1.7 |
| Ag | 0.5±0.2 | Ag | 7.7±3.3 |

The structure of the nanoparticles on the fiber surface was examined through XRD analysis, with the results shown in Fig. 5. The peaks in the PLA-TA-Ag A sample correspond to the crystalline structure of metallic silver (referenced by the JCPDS card of Ag NO. 04–0783 [44], whereas the peaks in

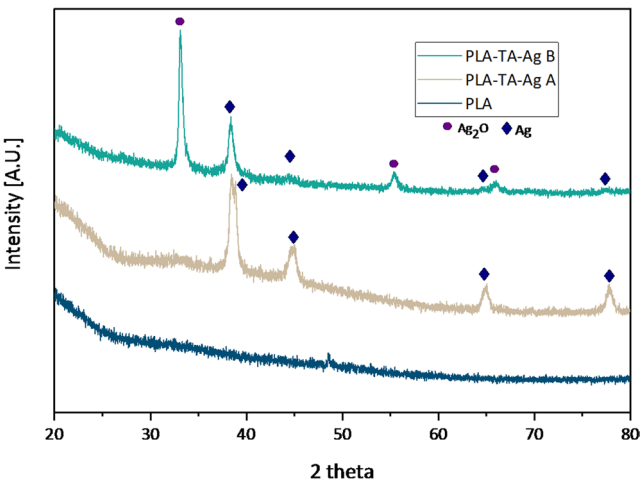


**Fig. 5** XRD patterns of PLA, PLA-TA-Ag A and PLA-TA-Ag B

the PLA-TA-Ag B sample can be attributed to both the crystalline structures of silver oxide and metallic silver ($Ag_2O$ reference and JCPDS card 01-1041 [45]), . The reducing ability of polyphenolic compounds is strongly influenced by the system's pH; a highly alkaline pH is necessary to fully deprotonate the hydroxyl groups, which are primarily responsible for reducing silver ions into metallic silver [41]. Unlike the authors' previous findings concerning the in situ reduction of AgNPs on clinoptilolite [32], where a pH of 8.5 enhanced silver ion reduction, the reduction is incomplete here, as silver oxide nanoparticles are also formed [46]. This may be related to the partial hydrolysis of PLA in contact with NaOH, which releases $H^+$, lowering the overall system pH and thus reducing the effectiveness of tannic acid's reducing capabilities [42, 43].

XPS was specifically employed to investigate the chemical state of AgNPs. The wide scans acquired in each sample (Figure S2) reveal the presence of Ag, C, and O, with the relative atomic concentrations reported in Table 2. The XPS results confirm the EDS findings regarding Ag concentrations, showing a higher amount in the PLA-TA-Ag B sample. C 1s and O 1s high-resolution spectra show the typical components of the chemical structure of the PLA matrix (Figures S3-S4). As regards silver analysis, the investigation on Ag 3d high-resolution spectra does not clarify the oxidation state of AgNPs. For each sample, the Ag 3d region (Figure S5) is characterized by a doublet in which the 5/2 component binding energy ranges in an interval of only 0.2 eV (368.0-368.2), even lower than the instrumental resolution (0.26 eV). Similarly, the full-width-at-half-maximum (FWHM) of each component of the doublet stays in the 0.9–1.1 eV range for all samples. In addition to that, the data reported in the literature do not show a clear shift of the binding energy between metallic and oxidized species, making the identification of the Ag oxidation state based on the 3d peak binding energy unreliable. In fact, according to the NIST (National Institute of Standards and Technology) X-ray Photoelectron Spectroscopy Database (SRD 20), Version 5.0 [47] the binding energy of the $3d_{5/2}$ component ranges from 367.9 to 368.4 eV for metallic Ag and from 367.7 to 368.4 eV for oxidized Ag (specifically $Ag_2O$). As a consequence, some works report a higher binding energy for the metal than the oxide [48] while others report the contrary [49]. All this considered, an analysis based on the fitting of the Ag 3d region to gain information about the oxidation state of AgNPs would be highly unreliable. Instead, the Ag MNN Auger region around 1135 eV in binding energy (Al $K_\alpha$ source) is known to have sufficiently different shape and shift between metallic and oxidized species to permit their identification [49].

**Table 2** Ag, C, and O relative atomic percentages (at%) of the PLA-TA-Ag A and B samples, calculated from Ag 3d, C 1s, and O 1s high-resolution spectra, respectively

| PLA-TA-Ag A | | PLA-TA-Ag B | |
|---|---|---|---|
| Element | % at | Element | % at |
| C | 70.5 | C | 70.5 |
| O | 28.9 | O | 26.0 |
| Ag | 0.6 | Ag | 3.5 |

First, Ag 3d and Ag Auger spectra were obtained from standard metallic Ag and $Ag_2O$ specimens (Figure S6), in order to have internal references to compare with our samples. The Ag 3d peaks of the two standards share the same binding energy (368.2 eV) and exhibit slightly different FWHM, i.e., 0.5 eV for the metal compared to 0.7 eV for the oxide, and shape, that is, asymmetric for the metal compared to Gaussian-Lorentzian for the oxide. These differences are not useful for the analysis of the samples, because the FWHM of all AgNPs 3d peaks is higher than that one of both standard samples. Instead, the structure of the Ag Auger regions can be used for the determination of the AgNPs oxidation state, as expected, according to the following procedure. First of all, the Auger regions were fitted of the two standards with a certain number of components, which have no specific chemical or physical meaning, but just help to reproduce the experimental trends. The best fits were achieved using seven components for the metal and four for the oxide (Figure SI 6b-d). For each region, these components were fixed in terms of binding energy position, FWHM, and relative intensities, in order to produce two different sets of data representing metal and oxide contributions, respectively. Subsequently, the Ag Auger regions of PLA-TA-Ag A and B were deconvoluted using these sets of peaks in a two-step procedure. First, the fitting was performed by varying only the overall intensity of each set of peaks, fixing all the other parameters. Second, the binding energy and FWHM of all the components were tuned in a narrow range, i.e., 0.2 eV around the starting value, to achieve the best overlap between the fitting and the experimental data, while the relative ratios of the components within each set were not varied.

In this way, the fitting of the Ag Auger regions of the samples is the result of a linear combination of the metal and oxide ($Ag_2O$) contributions, providing information about their presence and their relative atomic abundance in each sample, which was not possible from the analysis of Ag 3d regions.

The results of such procedure are shown in Fig. 6. The fittings confirm that in every sample there is the coexistence of metallic and oxidized Ag: their relative atomic concentrations, summarized in Table 3, are calculated from the total areas of the two different sets of peaks, one representing the metal contribution and the other representing the oxide contribution.

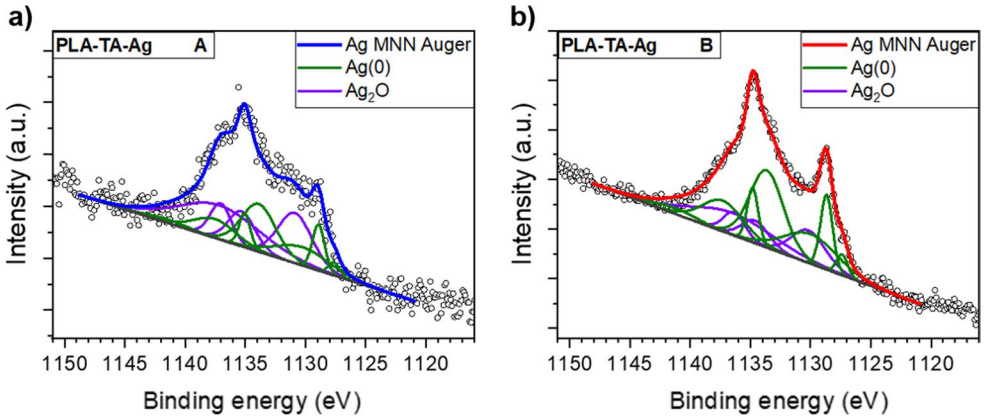


**Fig. 6** High-resolution Ag MNN Auger spectra of the PLA-TA-Ag A (**a**) and PLA-TA-Ag B (**b**) samples. The green components are related to the metallic Ag contribution, while the violet ones are related to the $Ag_2O$ contribution

**Table 3** Ag(0) and $Ag_2O$ relative atomic percentages (at%) in the PLA-TA-Ag A and PLA-TA-Ag B samples, calculated from the Ag Auger regions according to the method explained in the text

| Sample | at% Ag(0) | at% $Ag_2O$ |
|---|---|---|
| PLA-TA-Ag A | 43.1 | 56.9 |
| PLA-TA-Ag B | 64.8 | 35.2 |

It's important to notice that XPS is a surface-sensitive technique that provides the exact atomic composition and oxidation states at the surface, with a sampling depth of 10 nm at maximum from the sample surface [50]. As a result, its measurements are not directly comparable to those obtained from techniques such as XRD, which probe much deeper into the material, typically on the micrometer scale, yielding an "average" structural composition of the bulk material. For instance, XPS consistently detected a higher amount of oxidized silver in the sample PLA-TA-Ag A compared to XRD. This discrepancy can be attributed to the presence of a thin surface layer of air-oxidized silver on the AgNPs, likely too thin to be detected by XRD, as suggested in previous studies [51, 52].

## 3.2 Antibacterial activity evaluation of PLA-TA-Ag A and PLA-TA-Ag B

Antibacterial activity was assessed using a zone of inhibition test against *S. epidermidis*. As shown in Fig. 7, the control sample consisting of only PLA fluff exhibited no antibacterial activity, allowing bacterial colonies to grow around it. In contrast, the two functionalized samples demonstrated clear antibacterial efficacy against *S. epidermidis*. The antibacterial properties of metallic silver are well established [53], and $Ag_2O$ is also known for its effectiveness against various microorganisms [54]. The large bacteria-free zone observed in the PLA-TA-Ag B sample is undoubtedly due to the higher silver content detected by EDS, but the synergistic effect of metallic silver and silver oxide may also contribute to the enhanced antimicrobial activity of the sample [55]. For *E. coli*, a Gram-negative bacterium generally considered more resistant [56], the inhibition halo was clearly observed for PLA-TA-Ag B, whereas a smaller zone was detected for PLA-TA-Ag A (highlighted by the white arrows in Fig. 7b), consistent with the lower silver loading of this material. Given the high activity of $Ag_2O$ against *E. coli*, the pronounced inhibition zone observed for PLA-TA-Ag B is expected [57]. Notably, a "double" inhibition halo was observed, comprising (i) a well-defined inner region immediately surrounding the fluff that was completely free of bacterial growth and (ii) an outer, fainter region in which bacterial proliferation was reduced but not fully suppressed. Similar dual-halo patterns have been previously reported in the literature [58].

## 3.3 Physiochemical characterization of PLA-TA-Ag A and PLA-TA-Ag B after 30 days in water

FESEM analysis was conducted on the fibers after being soaked in Milli-Q water for 30 days. As shown in Fig. 8, the fibers remain well covered with nanoparticles, particularly those that underwent type B functionalization. This can be attributed to the effective functionalization of the PLA fibers with tannic acid, which is known for its stability in aqueous solutions over time [59].

EDS analysis was repeated after 30 days of soaking in Milli-Q water, and the outcomes are provided in Table 4. The silver content in the PLA-TA-Ag A sample appears unchanged, while a significant reduction is observed in the PLA-TA-Ag B sample. The oxidation state of silver plays a key role in the release kinetics of silver ions: according to the literature, the release of soluble silver involves a heterogeneous oxidation reaction. Consequently, if the nanoparticles are already oxidized, less energy is required to complete this reaction [60]. This phenomenon likely explains the changes in silver concentration after 30 days of immersion. In any case, the amount of silver observed after 30 days of immersion remains significant for the maintenance of antibacterial properties.

The XRD analysis results obtained after 30 days of water immersion are reported in Fig. 9 and confirm the findings from the EDS analysis (Table 4). After 30 days, both samples show the presence of only metallic silver. This is likely

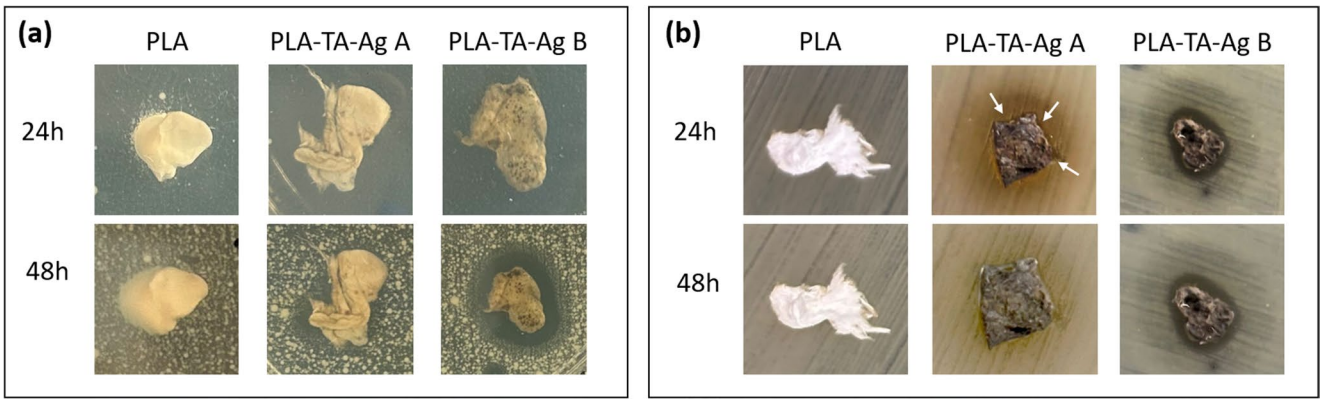


**Fig. 7** Zone of inhibition test against *S. epidermidis* (a) and *E. coli* (b) with PLA, PLA-TA-Ag A and PLA-TA-Ag B after 24 and 48 h of incubation

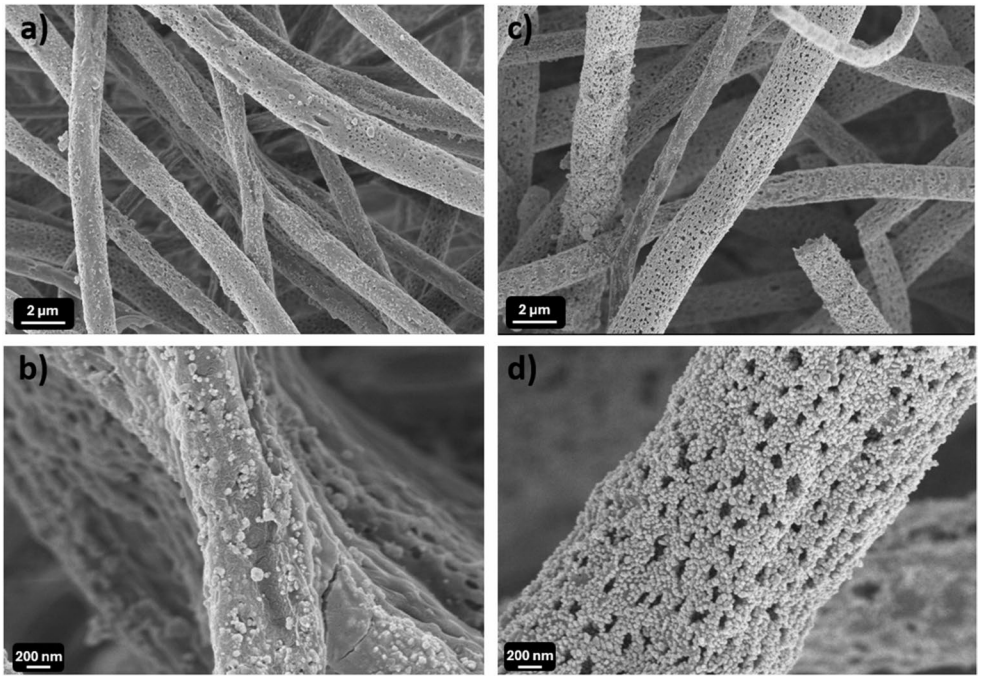


**Fig. 8** FESEM images of PLA-TA-Ag A (**a**, **b**) and PLA-TA-Ag B (**c**, **d**) after 30 days in water

because silver oxide rapidly releases silver ions, leaving only metallic silver in the PLA-TA-Ag B sample.

XPS analysis was also carried out on the samples after 30 days of immersion in Milli-Q water. The wide scan spectra (Figure S2) confirmed the presence of Ag, C, and O, with relative atomic concentrations reported in Table 5. The XPS results align with the EDS findings, showing a higher silver content in the PLA-TA-Ag B 30d sample, although both samples exhibited a decrease in Ag concentration compared to the initial condition (Table 2).

**Table 4** EDS analysis performed on PLA-TA-Ag A and PLA-TA-Ag B after 30 days in water

| PLA-TA-Ag A 30d | | PLA-TA-Ag B 30d | |
|---|---|---|---|
| Element | % at | Element | % at |
| C | 41.0±2.5 | C | 37.6±1.1 |
| O | 58.9±2.2 | O | 59.2±1.4 |
| Ag | 0.5±0.3 | Ag | 3.3±1.1 |

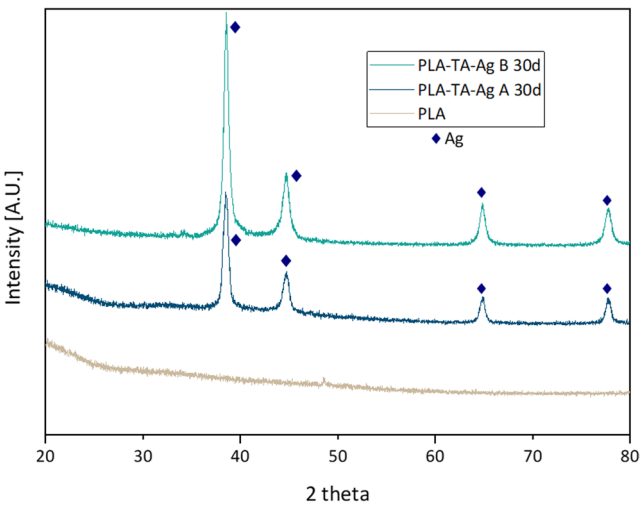


**Fig. 9** XRD patterns of PLA, PLA-TA-Ag A and PLA-TA-Ag B after 30 days in water

**Table 5** Ag, C, and O relative atomic percentages (at%) in the PLA-TA-Ag A 30d and PLA-TA-Ag B 30d, calculated from Ag 3d, C 1s, and O 1s high-resolution spectra, respectively

| PLA-TA-Ag A 30d | | PLA-TA-Ag B 30d | |
|---|---|---|---|
| Element | % at | Element | % at |
| C | 69.8 | C | 67.5 |
| O | 29.9 | O | 29.5 |
| Ag | 0.3 | Ag | 3.0 |

The high-resolution C 1s (Fig. S3) and O 1s spectra (Fig. S4) show the typical components of the PLA matrix, indicating the polymer's structural stability over time. In contrast, the Ag 3d spectra did not provide reliable information on the oxidation state of silver, as the $3d_{5/2}$ binding energy remained within a narrow 0.2 eV range (368.0–368.2 eV), which is smaller than the instrumental resolution (0.26 eV). Similarly, the FWHM of the peaks (0.9–1.1 eV) exceeded those observed in standard Ag and $Ag_2O$ references, making chemical state attribution through 3d analysis unreliable.

Therefore, the Ag MNN Auger region was analyzed using the fitting approach described in Sect. 3.1. The results, shown in Fig. 10, reveal a coexistence of metallic silver and silver oxide in both samples. The relative contributions, derived from the fitted Auger components (Table 6), indicate a notable decrease in silver oxide content after 30 days, particularly in sample PLA-TA-Ag A 30d, where metallic silver represents over 70% of the silver species.

These findings support the hypothesis that silver oxide dissolves more readily in water than metallic silver, leading to its preferential loss over time. Although XPS is a surface-sensitive technique with a maximum sampling depth of ~ 10 nm [50], and thus not directly comparable to bulk-sensitive methods like XRD, the results are consistent with other analyses and with literature reports describing the rapid solubilization of $Ag_2O$ under aqueous conditions [60].

The Milli-Q water in which the samples were stored for 30 days was analyzed to quantify the release of $Ag^+$ ions, with the results summarized in Table 7. Consistent with the EDS findings, a significantly higher silver ion concentration was detected in the PLA-TA-Ag B sample compared to PLA-TA-Ag A. This outcome aligns with the previously reported higher silver loading in sample B and suggests an enhanced release behavior associated with the greater content of oxidized silver species, which is known to dissolve more rapidly in aqueous environments.

**Table 6** Ag(0) and $Ag_2O$ relative atomic percentages (at%) in the PLA-TA-Ag A 30d and PLA-TA-Ag B 30d, calculated from the Ag Auger regions according to the method explained in the text

| Sample | at% Ag(0) | at% $Ag_2O$ |
|---|---|---|
| PLA-TA-Ag A 30d | 73.2 | 26.8 |
| PLA-TA-Ag B 30d | 51.8 | 48.2 |

**Table 7** Silver ion concentration ($Ag^+$, in ppm) measured in the Milli-Q water after 30 days of immersion of PLA-TA-Ag samples

| Sample | $Ag^+$ (ppm) |
|---|---|
| PLA-TA-Ag A | 0.345 |
| PLA-TA-Ag B | 5.500 |

## 3.4 Antibacterial activity evaluation of PLA-TA-Ag A 30d and PLA-TA-Ag B 30d

As shown in Fig. 11, a zone of inhibition test was also conducted on the samples after 30 days of soaking in Milli-Q water. As anticipated based on previous analyses, the samples retained their antibacterial properties, indicating their potential for applications in water-contact environments (Fig. 8). This sustained antibacterial effect even after prolonged immersion suggests a stable release mechanism of the active species. Notably, considering the comparative results obtained earlier in the study, it is plausible that antibacterial activity is more strongly linked to the presence of metallic silver rather than silver oxide. The persistence of inhibition zones implies that the metallic form of silver may play a dominant role in maintaining long-term antimicrobial efficacy [60], likely due to its slower oxidation and continuous surface activity. This highlights the importance of the silver speciation in designing materials for durable antimicrobial performance. As shown in Fig. 11b, the antibacterial

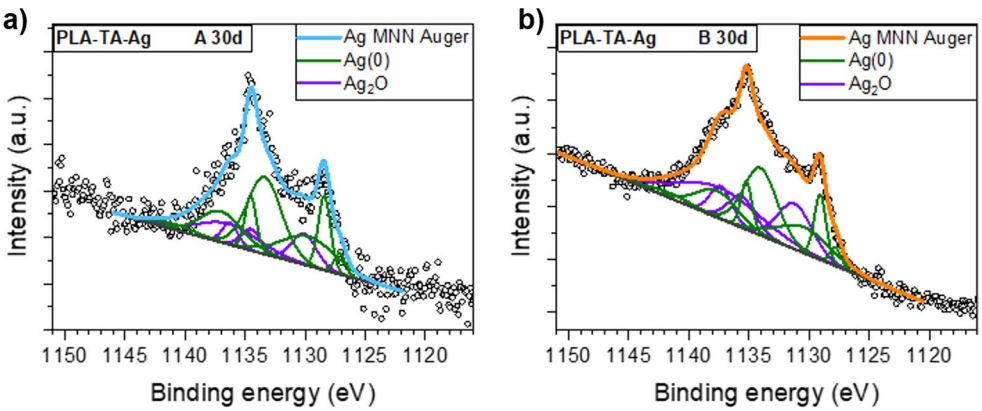


**Fig. 10** High-resolution Ag MNN Auger spectra of the PLA-TA-Ag A 30d (**a**) and PLA-TA-Ag B 30d (**b**) samples. The green components are related to the metallic Ag contribution, while the violet ones are related to the $Ag_2O$ contribution

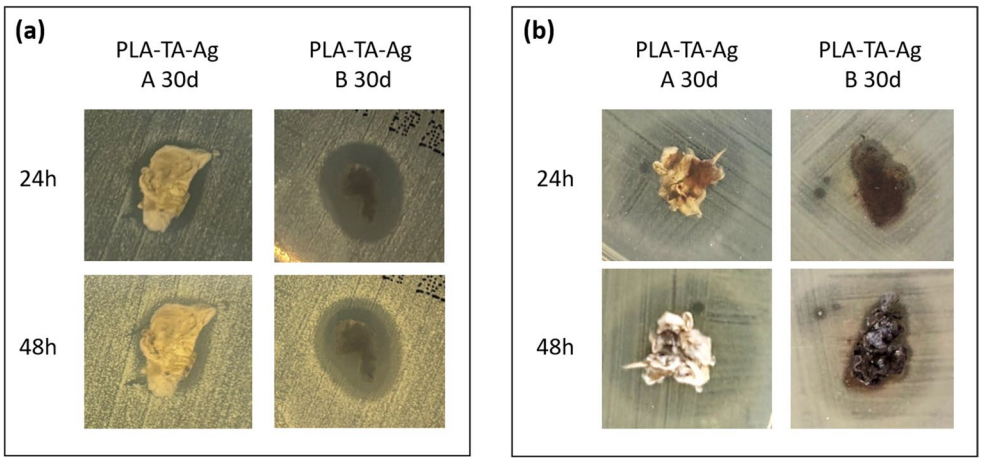


**Fig. 11** Zone of inhibition test against *S. epidermidis* (**a**) and *E. coli* (**b**) with PLA, PLA-TA-Ag A 30d and PLA-TA-Ag B 30d after 24 and 48 h of incubation

effect against *E. coli* is still detectable for both PLA-TA-Ag A and PLA-TA-Ag B, although it is less pronounced compared to what was observed for *S. epidermidis* in Fig. 11a.

### 3.5 Mechanical testing

In the perspective of developing antibacterial filtration devices capable of maintaining structural integrity in aqueous environments, the mechanical behavior of the fluffy monoliths was evaluated by uniaxial compression testing in water at T = 25 °C. Representative stress-strain curves are shown in Figs. 12a-b, while the main mechanical parameters are summarized in Table 8. All samples display the characteristic compressive response of highly porous fibrous networks, consisting of an initial quasi-linear elastic region, followed by progressive fibre rearrangement and packing, and a final densification regime associated with extensive compaction of the fibrous assembly [61].

The initial elastic modulus ($E_0$) ranged between 0.1 and 0.23 MPa, reflecting the extremely compliant nature of the highly porous fibrous structure. The densification modulus ($E_F$), ranging from 765 to 1815 MPa, describes the stiffness of the compacted fiber network and is governed by the density of inter-fiber contacts, structural connectivity and nanoparticle loading. The maximum strain ($\varepsilon_{max}$), reaching values as high as 84–98%, confirms the extremely high initial porosity of the monoliths, in agreement with their fluffy morphology. Differences in $E_F$ and $\varepsilon_{max}$ among samples reflect variations in fiber packing density and interconnectivity, with more compact architectures exhibiting higher resistance to compression. The maximum stress values ($\sigma_{max}$), ranging from 46.8 to 93.6 MPa, further confirm the mechanical robustness of the compacted fibrous network.

From an application standpoint, the most relevant parameters are the compressive strains corresponding to the typical operating pressure range used in aqueous filtration systems (0.5–0.6 bar) [62]. As visible in Fig. 12b, under these conditions, all samples exhibited limited deformation, corresponding to approximately 22–28% strain. This moderate compaction indicates that the fibrous architecture

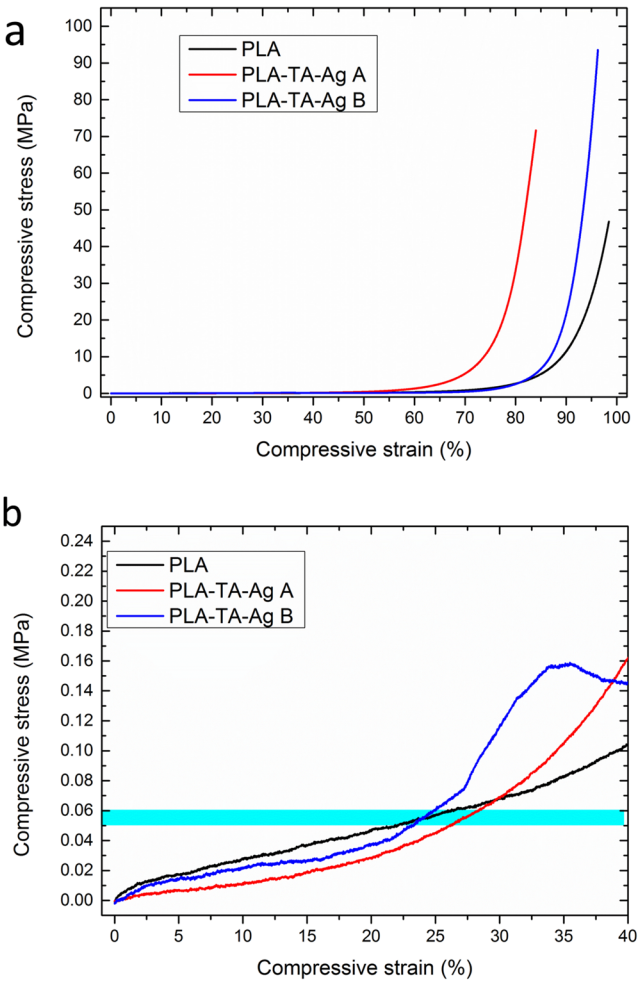


**Fig. 12** Representative compressive stress-strain curves of the fluffy monoliths in the full range (**a**) and in the stress–strain region corresponding to the operating pressure range (0.5–0.6 bar) (**b**)

**Table 8** Mechanical parameters of fluffy monoliths obtained from compression testing

| Property | PLA | PLA-TA-Ag A | PLA-TA-Ag B |
|---|---|---|---|
| $E_0$ (MPa) | 0.23 ± 0.02 | 0.11 ± 0.03 | 0.21 |
| $E_F$ (MPa) | 765 ± 18 | 1100 ± 12 | 1815 ± 25 |
| $\varepsilon_D$ (%) | 87.2 ± 0.8 | 73.7 ± 1.2 | 86.7 ± 0.7 |
| $\sigma_D$ (MPa) | 0.21 ± 0.1 | 0.08 ± 0.0 | 0.18 ± 0.0 |
| $\sigma_{max}$ (MPa) | 46.8 ± 1.5 | 71.6 ± 0.1 | 93.6 ± 0.1 |
| $\varepsilon_{max}$ (%) | 98.4 ± 0.2 | 84.0 ± 0.4 | 96.3 ± 0.1 |
| Energy at $\varepsilon_{max}$ (MJ/m$^3$) | 2.96 ± 0.1 | 3.94 ± 0.1 | 4.22 ± 0.1 |
| ε at 0.5 bar (%) | 22.0 ± 0.1 | 26.2 ± 0.1 | 23.3 ± 0.1 |
| ε at 0.6 bar (%) | 26.4 ± 0.2 | 28.3 ± 0.9 | 25.0 ± 0.4 |

maintains high porosity and structural integrity during operation, with deformation occurring primarily through reversible fibre rearrangement rather than structural collapse [61, 63]. These results demonstrate that the developed fluffy monoliths possess sufficient mechanical stability for filtration applications, operating well below the high-compaction regime identified at significantly higher stress levels.

### 3.6 Antimicrobial filtration test

To assess the antimicrobial performance of the functionalized fluff under flowing-water conditions, a bench-scale dead-end filtration setup was assembled and operated following the procedure described by *Park et al.* [37]. The log reduction values (LRV) calculated from the bacterial concentration in the permeate for PLA, PLA-TA-Ag A, and PLA-TA-Ag B are reported in Fig. 13a. Neat PLA exhibited modest LRV values (0.82 for the first 20 mL and 0.69 for the final aliquot), with an overall decreasing trend. Although PLA is not expected to provide intrinsic antibacterial activity, the observed reduction is likely attributable to physical retention of *S. epidermidis* within the fibrous matrix, considering the characteristic cell size relative to the pore size of the fibers [64]. Functionalization with TA/Ag improved bacterial removal. PLA-TA-Ag A showed LRV > 1 for the first 20 mL and remained around 0.8 in the last aliquot. A markedly higher reduction was achieved by PLA-TA-Ag B, consistent with its increased silver loading resulting from the higher pH employed during functionalization: the LRV was 4.2 in the first 20 mL and decreased to 2.2 in the final aliquot. This less stable behavior is plausibly associated with a rapid initial release of Ag species present in the sample [60]. Because retained bacteria may remain viable and proliferate on the filter over time, potentially turning the filter into a secondary contamination source [65, 66], the filtered samples were recovered after testing and incubated on agar plates to evaluate post-filtration bacterial growth (Fig. 13b). As shown in Fig. 13b, both silver-functionalized samples exhibited no detectable bacterial growth after 24 h, indicating that bacteria retained within the filter were effectively inactivated by silver at the fiber surface. In contrast, the PLA control showed multiple colonies surrounding the fluff after 24 h of incubation (highlighted by white arrows in Fig. 13b), demonstrating that physical retention alone is insufficient to prevent regrowth and underscoring the need to incorporate an antibacterial agent into the filter to inhibit proliferation and potential downstream release.

The filtrate was further analyzed to quantify $Ag^+$ release and assess the practical applicability of the materials in real water filtration systems. At the end of the filtration test, the $Ag^+$ concentration measured for PLA-TA-Ag A was 28.07 ± 2.23 ppb, whereas PLA-TA-Ag B released 106.65 ± 6.50 ppb.

According to the World Health Organization (WHO), the guideline value for silver in drinking water is 100 ppb [67]. Notably, PLA-TA-Ag A, functionalized at lower pH and

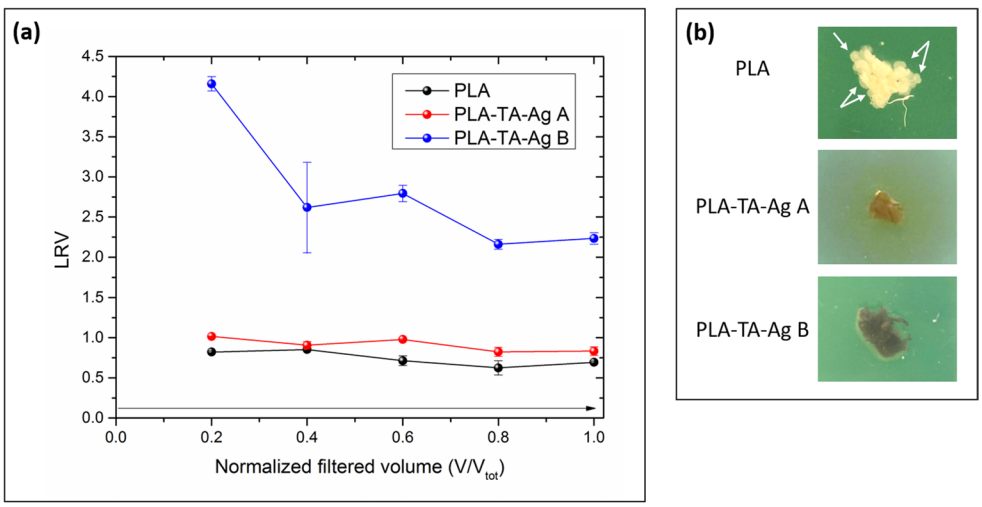


**Fig. 13** Log removal value (LRV) of *Staphylococcus epidermidis* obtained for PLA, PLA-TA-Ag A, and PLA-TA-Ag B during the antimicrobial filtration test (**a**), along with images of PLA, PLA-TA-Ag A, and PLA-TA-Ag B after 24 h incubation following the antimicrobial filtration test (**b**)

characterized by predominantly metallic silver, released $Ag^+$ concentrations well below this safety threshold while still exhibiting antibacterial activity, highlighting a favorable balance between efficacy and limited ion release. PLA-TA-Ag B, produced under alkaline conditions and containing higher silver loading (including $Ag_2O$), showed a higher release close to the recommended limit. Overall, these two materials can be considered as representative lower and upper bounds of a pH-tunable functionalization window, demonstrating that silver content and release can be readily modulated through pH control to meet application-specific performance and safety requirements.

## 4 Conclusions

This study demonstrated a green and effective strategy for fabricating antimicrobial fibrous scaffolds by combining wet electrospinning of poly(lactic acid) (PLA) with in situ functionalization using tannic acid-mediated silver reduction. The process enabled the formation of porous, three-dimensional PLA fluffs with high surface area, suitable for filtration applications. Two different pH conditions during silver functionalization significantly influenced the morphology, silver content, and composition of the deposited nanoparticles.

Physicochemical characterizations confirmed successful functionalization, with higher silver loading and the formation of both Ag and $Ag_2O$ nanoparticles under alkaline conditions. Importantly, antibacterial assays against *Staphylococcus epidermidis* and *Escherichia coli* revealed strong antimicrobial efficacy for both functionalized samples, with enhanced performance observed in the more heavily loaded, alkaline-treated material. Furthermore, the materials retained their structural integrity and antimicrobial activity after 30 days of immersion in water, confirming their long-term stability and functionality in humid or aqueous environments. Dynamic water filtration tests, supported by uniaxial compression measurements under aqueous conditions, further demonstrated their practical applicability by combining effective bacterial removal/inactivation in the permeate with adequate mechanical robustness, particularly for the high-silver-loading sample. Overall, the developed PLA–Ag nanohybrid fluffs represent a promising and sustainable solution for next-generation antimicrobial filters in applications ranging from personal protective equipment to air and water purification systems. Future work may focus on scaling the process and evaluating the materials' performance against a broader range of microbial contaminants and in real-world conditions.

**Supplementary Information** The online version contains supplementary material available at https://doi.org/10.1007/s42114-026-01733-7.

**Author contributions** Conceptualization, M.M., R.S., A.M.; Methodology, F.G., M.L., M.M., A.M., R.S.; Investigation, F.G., M.L., M.M., A.M., F.D.B., M.P.; Resources, M.M., R.S.; Writing-original draft preparation, F.G, M.M., A.M.; Writing-review and editing, F.G., M.M., A.M., R.S, F.D.B., M.P.; Visualization, F.G., A.M.; Supervision, M.M.; Project administration, M.M., R.S.; Funding acquisition, M.M., R.S. All authors have read and agreed to the published version of the manuscript.

**Funding** Open access funding provided by Università degli Studi di Palermo within the CRUI-CARE Agreement. This study was carried out within the MICS (Made in Italy – Circular and Sustainable) Extended Partnership and received funding from the European Union Next-Generation EU (PIANO NAZIONALE DI RIPRESA E RESILIENZA (PNRR) – MISSIONE 4 COMPONENTE 2, INVESTIMENTO 1.3 – D.D. 1551.11-10-2022, PE00000004). This manuscript reflects only the authors' views and opinions, neither the European Union nor the European Commission can be considered responsible for them. A.M. and R.S. also received funding from ECOROADS - barriere innovative per la mitigazione dell'inquinamento acustico e chimicogenerato dalle strade, ARS01_00752, DD1735/17, DD1241/2021, CUP: B75F21000570005.

**Data availability** The datasets generated and analyzed during the current study are available from the corresponding authors on reasonable requests.

## Declarations

**Competing interests** The authors declare no competing interests.

**Open Access** This article is licensed under a Creative Commons Attribution 4.0 International License, which permits use, sharing, adaptation, distribution and reproduction in any medium or format, as long as you give appropriate credit to the original author(s) and the source, provide a link to the Creative Commons licence, and indicate if changes were made. The images or other third party material in this article are included in the article's Creative Commons licence, unless indicated otherwise in a credit line to the material. If material is not included in the article's Creative Commons licence and your intended use is not permitted by statutory regulation or exceeds the permitted use, you will need to obtain permission directly from the copyright holder. To view a copy of this licence, visit http://creativecommons.org/licenses/by/4.0/.

## References

1. Tropea A (2022) Microbial Contamination and Public Health: An Overview. IJERPH 19:7441. https://doi.org/10.3390/ijerph19127441
2. Kristanti RA, Hadibarata T, Syafrudin M, Yılmaz M, Abdullah S (2022) Microbiological Contaminants in Drinking Water: Current Status and Challenges. Water Air Soil Pollut 233. https://doi.org/10.1007/s11270-022-05698-3
3. Meade E, Slattery MA, Garvey M (2021) Biocidal Resistance in Clinically Relevant Microbial Species: A Major Public Health Risk. Pathogens 10:598. https://doi.org/10.3390/pathogens10050598
4. Moccia G, Motta O, Pironti C, Proto A, Capunzo M, De Caro F (2020) An alternative approach for the decontamination of hospital settings. J Infect Public Health 13:2038–2044. https://doi.org/10.1016/j.jiph.2020.09.020
5. Portier CJ, Health CEP (2011) Public Health Rep 126:3–6. https://doi.org/10.1177/00333549111260s102
6. Ma J-Y, Li M-Y, Qi Z-Z, Fu M, Sun T-F, Elsheikha HM, Cong W (2022) Waterborne protozoan outbreaks: An update on the global,

regional, and national prevalence from 2017 to 2020 and sources of contamination. Sci Total Environ 806:150562. https://doi.org/10.1016/j.scitotenv.2021.150562
7. Fernstrom A, Goldblatt M (2013) Aerobiology and Its Role in the Transmission of Infectious Diseases. J Pathog 2013:493960. https://doi.org/10.1155/2013/493960
8. Wang CC, Prather KA, Sznitman J, Jimenez JL, Lakdawala SS, Tufekci Z, Marr LC (2021) Airborne transmission of respiratory viruses. Science 373. https://doi.org/10.1126/science.abd9149
9. Elsaid AM, Ahmed MS (2021) Indoor Air Quality Strategies for Air-Conditioning and Ventilation Systems with the Spread of the Global Coronavirus (COVID-19) Epidemic: Improvements and Recommendations. Environ Res 199:111314. https://doi.org/10.1016/j.envres.2021.111314
10. Maung TZ, Bishop JE, Holt E, Turner AM, Pfrang C (2022) Indoor Air Pollution and the Health of Vulnerable Groups: A Systematic Review Focused on Particulate Matter (PM), Volatile Organic Compounds (VOCs) and Their Effects on Children and People with Pre-Existing Lung Disease. Int J Environ Res Public Health 19:8752. https://doi.org/10.3390/ijerph19148752
11. Myung H, Joung YS (2024) Contribution of Particulates to Airborne Disease Transmission and Severity: A Review, Environ. Sci Technol 58:6846–6867. https://doi.org/10.1021/acs.est.3c08835
12. Brainard J, Jones NR, Swindells IC, Archer EJ, Kolyva A, Letley C, Pond K, Lake IR, Hunter PR (2023) Effectiveness of filtering or decontaminating air to reduce or prevent respiratory infections: A systematic review. Prev Med 177:107774. https://doi.org/10.1016/j.ypmed.2023.107774
13. Cevallos-Mendoza J, Amorim C, Rodríguez-Díaz J, Montenegro M (2022) Removal of Contaminants from Water by Membrane Filtration: A Review. Membranes 12:570. https://doi.org/10.3390/membranes12060570
14. Aswathy NR, Divakaran N, Ajay Kumar PV, Kumar A, Sudha GS, Mohanty S, Palai AK (2024) Swifty fabrication of 3D multifunctional porous green polymer monoliths for supercapacitor electrodes and water purification applications. J Energy Storage 84:110946. https://doi.org/10.1016/j.est.2024.110946
15. Lyu C, Zhao P, Xie J, Dong S, Liu J, Rao C, Fu J (2021) Electrospinning of Nanofibrous Membrane and Its Applications in Air Filtration: A Review. Nanomaterials 11:1501. https://doi.org/10.3390/nano11061501
16. Makaremi M, De Silva RT, Pasbakhsh P (2015) Electrospun Nanofibrous Membranes of Polyacrylonitrile/Halloysite with Superior Water Filtration Ability. J Phys Chem C 119:7949–7958. https://doi.org/10.1021/acs.jpcc.5b00662
17. Mihut DM, Afshar A, Lackey LW, Le KN (2019) Antibacterial effectiveness of metallic nanoparticles deposited on water filter paper by magnetron sputtering. Surf Coat Technol 368:59–66. https://doi.org/10.1016/j.surfcoat.2019.04.039
18. Mamun A, Blachowicz T, Sabantina L (2021) Electrospun Nanofiber Mats for Filtering Applications—Technology, Structure and Materials. Polymers 13:1368. https://doi.org/10.3390/polym13091368
19. Scaffaro R, Gammino M, Maio A (2022) Wet electrospinning-aided self-assembly of multifunctional GO-CNT@PCL core-shell nanocomposites with spider leg bioinspired hierarchical architectures. Compos Sci Technol 221:109363. https://doi.org/10.1016/j.compscitech.2022.109363
20. MaioA,Gammino M, Gulino EF, Megna B, Fara P, Scaffaro R (2020) Rapid one-step fabrication of graphene oxide-decorated polycaprolactone three-dimensional templates for water treatment. ACS Appl Polym Mater 2:4993–5005. https://doi.org/10.1021/acsapm.0c00852
21. Liao K-H, Ou K-L, Cheng H-C, Lin C-T, Peng P-W (2010) Effect of silver on antibacterial properties of stainless steel. Appl Surf Sci 256:3642–3646. https://doi.org/10.1016/j.apsusc.2010.01.001
22. Yin IX, Zhang J, Zhao IS, Mei ML, Li Q, Chu CH (2020) The Antibacterial Mechanism of Silver Nanoparticles and Its Application in Dentistry. IJN Volume 15:2555–2562. https://doi.org/10.2147/IJN.S246764
23. More PR, Pandit S, Filippis AD, Franci G, Mijakovic I, Galdiero M (2023) Silver Nanoparticles: Bactericidal and Mechanistic Approach against Drug Resistant Pathogens. Microorganisms 11:369. https://doi.org/10.3390/microorganisms11020369
24. Luceri A, Francese R, Lembo D, Ferraris M, Balagna C (2023) Silver Nanoparticles: Review of Antiviral Properties, Mechanism of Action and Applications. Microorganisms 11:629. https://doi.org/10.3390/microorganisms11030629
25. Vanlalveni C, Lallianrawna S, Biswas A, Selvaraj M, Changmai B, Lalthazuala S, Rokhum (2021) Green synthesis of silver nanoparticles using plant extracts and their antimicrobial activities: a review of recent literature. RSC Adv 11:2804–2837. https://doi.org/10.1039/D0RA09941D
26. Swilam N, Nematallah KA (2020) Polyphenols profile of pomegranate leaves and their role in green synthesis of silver nanoparticles. Sci Rep 10. https://doi.org/10.1038/s41598-020-71847-5
27. Kim TY, Cha S-H, Cho S, Park Y (2016) Tannic acid-mediated green synthesis of antibacterial silver nanoparticles. Arch Pharm Res 39:465–473. https://doi.org/10.1007/s12272-016-0718-8
28. Gülçin İ, Huyut Z, Elmastaş M, Aboul-Enein HY (2010) Radical scavenging and antioxidant activity of tannic acid. Arab J Chem 3:43–53. https://doi.org/10.1016/j.arabjc.2009.12.008
29. Zhang A, Xiao Y, Das P, Zhang L, Zhang Y, Fang H, Wang L, Cao Y (2019) Synthesis, dissolution, and regeneration of silver nanoparticles stabilized by tannic acid in aqueous solution. J Nanopart Res 21. https://doi.org/10.1007/s11051-019-4563-9
30. Kaczmarek B (2020) Tannic Acid with Antiviral and Antibacterial Activity as A Promising Component of Biomaterials—A Minireview. Materials 13:3224. https://doi.org/10.3390/ma13143224
31. Syukri DM, Nwabor OF, Singh S, Voravuthikunchai SP (2021) Antibacterial functionalization of nylon monofilament surgical sutures through in situ deposition of biogenic silver nanoparticles. Surf Coat Technol 413:127090. https://doi.org/10.1016/j.surfcoat.2021.127090
32. Gattucci F, Lallukka M, Grifasi N, Piumetti M, Miola M (2025) Tannic acid-assisted green functionalization of Clinoptilolite: A step-by-step characterization of silver nanoparticles in situ reduction. Ceram Int S0272884225001622. https://doi.org/10.1016/j.ceramint.2025.01.151
33. Zhao J, Liu Y, Pan B, Gao G, Liu Y, Liu S, Liang N, Zhou D, Vijver MG, Peijnenburg WJGM (2017) Tannic acid promotes ion release of copper oxide nanoparticles: Impacts from solution pH change and complexation reactions. Water Res 127:59–67. https://doi.org/10.1016/j.watres.2017.10.006
34. Khodadadi B, Bordbar M, Yeganeh-Faal A, Nasrollahzadeh M (2017) Green synthesis of Ag nanoparticles/clinoptilolite using Vaccinium macrocarpon fruit extract and its excellent catalytic activity for reduction of organic dyes. J Alloys Compd 719:82–88. https://doi.org/10.1016/j.jallcom.2017.05.135
35. Fairley N, Fernandez V, Richard-Plouet M, Guillot-Deudon C, Walton J, Smith E, Flahaut D, Greiner M, Biesinger M, Tougaard S, Morgan D, Baltrusaitis J (2021) Systematic and collaborative approach to problem solving using X-ray photoelectron spectroscopy. Appl Surf Sci Adv 5:100112. https://doi.org/10.1016/j.apsadv.2021.100112
36. NCCLS M2-A9 (2003) Performance Standards for Antimicrobial Disk Susceptibility Tests, Approved Standard, 9th edn. NCCLS, Villanova, PA. (n.d.)
37. Park J-A, Kim S-B (2017) Antimicrobial filtration with electrospun poly(vinyl alcohol) nanofibers containing benzyl triethylammonium chloride: Immersion, leaching, toxicity, and filtration tests. Chemosphere 167:469–477. https://doi.org/10.1016/j.chemosphere.2016.10.030

38. Gulzar S, Tagrida M, Nilsuwan K, Prodpran T, Benjakul S (2022) Electrospinning of gelatin/chitosan nanofibers incorporated with tannic acid and chitooligosaccharides on polylactic acid film: Characteristics and bioactivities. Food Hydrocolloids 133:107916. https://doi.org/10.1016/j.foodhyd.2022.107916
39. Chen Y, Lin J, Fei Y, Wang H, Gao W (2010) Preparation and characterization of electrospinning PLA/curcumin composite membranes. Fibers Polym 11:1128–1131. https://doi.org/10.1007/s12221-010-1128-z
40. Sainz-Urruela C, Vera-López S, Paz San Andrés M, Díez-Pascual AM (2022) Surface functionalization of graphene oxide with tannic acid: Covalent vs non-covalent approaches. J Mol Liq 357:119104. https://doi.org/10.1016/j.molliq.2022.119104
41. Ahmad T (2014) Reviewing the Tannic Acid Mediated Synthesis of Metal Nanoparticles. J Nanatechnol 2014:1–11. https://doi.org/10.1155/2014/954206
42. Ranjbar Mohammadi M, Naghashzargar E, Kamali Moghaddam M, Khorshidi R (2024) Production of PLA fibers with surface modifications and silver nanoparticle coating to impart antibacterial activity. Polym Bull 81:6055–6072. https://doi.org/10.1007/s00289-023-04989-x
43. Schneider M, Fritzsche N, Puciul-Malinowska A, Baliś A, Mostafa A, Bald I, Zapotoczny S, Taubert A (2020) Surface Etching of 3D Printed Poly(lactic acid) with NaOH: A Systematic Approach. Polymers 12:1711. https://doi.org/10.3390/polym12081711
44. Dilshad E, Bibi M, Sheikh NA, Tamrin KF, Mansoor Q, Maqbool Q, Nawaz M (2020) Synthesis of functional silver nanoparticles and microparticles with modifiers and evaluation of their antimicrobial, anticancer, and antioxidant activity, JFB 11 76. https://doi.org/10.3390/jfb11040076
45. Wang T, Xiao H, Gao Y, Xu J, Zhang Z, Bian H, Sun T (2020) Ag2O/TiO2 hollow microsphere heterostructures with exposed high-energy {001} crystal facets and high photocatalytic activities. J Mater Sci: Mater Electron 31:11496–11507. https://doi.org/10.1007/s10854-020-03697-w
46. Salgado P, Bustamante L, Carmona DJ, Meléndrez MF, Rubilar O, Salazar C, Pérez AJ, Vidal G (2023) Green synthesis of Ag/Ag2O nanoparticles on cellulose paper and cotton fabric using Eucalyptus globulus leaf extracts: Toward the clarification of formation mechanism. Surf Interfaces 40:102928. https://doi.org/10.1016/j.surfin.2023.102928
47. Lee AY, Powell CJ, Gorham JM, Morey A, Scott JHJ, Hanisch RJ (2024) Development of the NIST X-ray Photoelectron Spectroscopy (XPS) Database, Version 5. CODATA 23 45. https://doi.org/10.5334/dsj-2024-045
48. Gaarenstroom SW, Winograd N (1977) Initial and final state effects in the ESCA spectra of cadmium and silver oxides. J Chem Phys 67:3500–3506. https://doi.org/10.1063/1.435347
49. Ferraria AM, Carapeto AP, Botelho Do Rego AM (2012) X-ray photoelectron spectroscopy: Silver salts revisited. Vacuum 86:1988–1991. https://doi.org/10.1016/j.vacuum.2012.05.031
50. Greczynski G, Haasch RT, Hellgren N, Lewin E, Hultman L (2023) X-ray photoelectron spectroscopy of thin films. Nat Rev Methods Primers 3. https://doi.org/10.1038/s43586-023-00225-y
51. Mohamedkhair AK, Drmosh QA, Yamani ZH (2019) Silver Nanoparticle-Decorated Tin Oxide Thin Films: Synthesis, Characterization, and Hydrogen Gas Sensing. Front Mater 6. https://doi.org/10.3389/fmats.2019.00188
52. Matsushima S, Teraoka Y, Miura N, Yamazoe N (1988) Electronic Interaction between Metal Additives and Tin Dioxide in Tin Dioxide-Based Gas Sensors. Jpn J Appl Phys 27:1798. https://doi.org/10.1143/jjap.27.1798
53. Bruna T, Maldonado-Bravo F, Jara P, Caro N (2021) Silver Nanoparticles and Their Antibacterial Applications. IJMS 22:7202. https://doi.org/10.3390/ijms22137202
54. Gudkov SV, Serov DA, Astashev ME, Semenova AA, Lisitsyn AB (2022) Ag2O Nanoparticles as a Candidate for Antimicrobial Compounds of the New Generation. Pharmaceuticals 15:968. https://doi.org/10.3390/ph15080968
55. Pandey M, Singh M, Wasnik K, Gupta S, Patra S, Gupta PS, Pareek D, Chaitanya NSN, Maity S, Reddy ABM, Tilak R, Paik P (2021) Targeted and Enhanced Antimicrobial Inhibition of Mesoporous ZnO–$Ag_2O$/Ag, ZnO–CuO, and ZnO–$SnO_2$ Composite Nanoparticles. ACS Omega 6:31615–31631. https://doi.org/10.1021/acsomega.1c04139
56. Graves JL, Tajkarimi M, Cunningham Q, Campbell A, Nonga H, Harrison SH, Barrick JE (2015) Rapid evolution of silver nanoparticle resistance in Escherichia coli. Front Genet 6. https://doi.org/10.3389/fgene.2015.00042
57. Li D, Chen S, Zhang K, Gao N, Zhang M, Albasher G, Shi J, Wang C (2021) The interaction of Ag2O nanoparticles with Escherichia coli: inhibition–sterilization process. Sci Rep 11:1703. https://doi.org/10.1038/s41598-021-81305-5
58. Mollea C, Bosco F, Fissore D (2022) Agar Plate Methods for Assessing the Antibacterial Activity of Thyme and Oregano Essential Oils against S. epidermidis and E. coli. Antibiotics 11:1809. https://doi.org/10.3390/antibiotics11121809
59. Abouelmagd SA, Meng F, Kim B-K, Hyun H, Yeo Y (2016) Tannic Acid-Mediated Surface Functionalization of Polymeric Nanoparticles, ACS Biomater. Sci Eng 2:2294–2303. https://doi.org/10.1021/acsbiomaterials.6b00497
60. Bonilla-Gameros L, Chevallier P, Copes F, Sarkissian A, Mantovani D (2022) The oxidation state of Ag nanoparticles highly affects the release of Ag ions without compromising the mechanical performance and the safety of amorphous hydrogenated carbon coatings. Diam Relat Mater 130:109430. https://doi.org/10.1016/j.diamond.2022.109430
61. Wang H, Cheng L, Yu J, Si Y (2025) Self-adaptable mechanical ceramic fibrous aerogels from prestressed topology and multistable constraints. Nat Commun 16:6885. https://doi.org/10.1038/s41467-025-62164-4
62. Pronk W, Ding A, Morgenroth E, Derlon N, Desmond P, Burkhardt M, Wu B, Fane AG (2019) Gravity-driven membrane filtration for water and wastewater treatment: A review. Water Res 149:553–565. https://doi.org/10.1016/j.watres.2018.11.062
63. Zong D, Zhang X, Yin X, Wang F, Yu J, Zhang S, Ding B (2022) Electrospun Fibrous Sponges: Principle, Fabrication, and Applications. Adv Fiber Mater 4:1434–1462. https://doi.org/10.1007/s42765-022-00202-2
64. Supragingival Microbes, in (2015) Atlas of Oral Microbiology. Elsevier, pp 41–65. https://doi.org/10.1016/B978-0-12-802234-4.00003-3
65. Ribeiro B, Vázquez-López A, Vazquez-Pufleau M, Llamosí M, Sempere J, Yuste J, Domenech M, Wang D-Y, Vilatela JJ, Llorca J, Echeverry-Rendón M (2024) Control of microbial agents by functionalization of commercial air filters with metal oxide particles. Mater Chem Phys 313:128684. https://doi.org/10.1016/j.matchemphys.2023.128684
66. Nriagu J, Xi C, Siddique A, Vincent A, Shomar B (2018) Influence of Household Water Filters on Bacteria Growth and Trace Metals in Tap Water of Doha, Qatar. Sci Rep 8:8268. https://doi.org/10.1038/s41598-018-26529-8
67. Rosa LR, Rosa RD, Da MAMS, Veiga (2016) Colloidal silver and silver nanoparticles bioaccessibility in drinking water filters. J Environ Chem Eng 4:3451–3458. https://doi.org/10.1016/j.jece.2016.07.017


**Publisher's note** Springer Nature remains neutral with regard to jurisdictional claims in published maps and institutional affiliations.